Commun. Comput. Phys.
doi: 10.4208/cicp.OA-2024-0285

Vol. **39**, No. 1, pp. 215-239
January 2026

Total Variation Distance-Enhanced Selective Segmentation for Medical Images

Po-Wen Hsieh[1], Chung-Lin Tseng[2] and Suh-Yuh Yang[3,*]

[1] *Department of Applied Mathematics, National Chung Hsing University, South District, Taichung City 402202, Taiwan.*
[2] *Department of Mathematics, National Tsing Hua University, Hsinchu City 300044, Taiwan.*
[3] *Department of Mathematics, National Central University, Jhongli District, Taoyuan City 320317, Taiwan.*

Received 22 November 2024; Accepted (in revised version) 3 May 2025

Abstract. In this paper, we propose an enhanced local intensity clustering energy functional designed for selective segmentation of medical images, particularly those affected by intensity inhomogeneity. The functional includes an area constraint term based on a total variation (TV) distance function derived from the single-scale Retinex output image. This TV distance function measures an unusual distance between points in the image domain and specified marker points, ensuring accurate localization of the selected objects. By combining this with local intensity clustering fitting energy and contour length regularization, the resulting minimization model achieves precisely selective segmentation and tight object wrapping. Moreover, instead of solving the Euler-Lagrange equation or using the level set method, we introduce an efficient iterative convolution-thresholding method to implement the model numerically. This method guarantees energy decay and enables faster convergence to a stable partition. Numerical experiments on some medical images demonstrate the effectiveness and efficiency of our proposed approach for selective image segmentation.

AMS subject classifications: 68U10, 65K10

Key words: Selective image segmentation, medical image, intensity inhomogeneity, single-scale Retinex, iterative convolution-thresholding method.

1 Introduction

Selective image segmentation is a targeted approach that extracts specific objects from an image with the help of some prescribed marker points placed near or within the regions

*Corresponding author. *Email addresses:* pwhsieh@nchu.edu.tw (P.-W. Hsieh), tseng0920@gapp.nthu.edu.tw (C.-L. Tseng), syyang@math.ncu.edu.tw (S.-Y. Yang)

of interest, which is crucial for medical imaging applications such as lesion and tumor detection. This method contrasts with global segmentation techniques, which attempt to divide the entire image into distinct regions by isolating all foreground objects that differ from the background. It also differs from interactive segmentation, where more extensive user input is required compared to the fewer inputs in selective segmentation [3,11,34]. By concentrating on specific areas of interest, selective segmentation achieves greater accuracy and efficiency, making it particularly valuable in medical imaging applications.

Over the past decades, variational methods have become an essential approach in image segmentation due to their ability to incorporate prior knowledge and constraints into the process [1,27]. These methods typically fall into two main categories: edge-based and region-based models. Edge-based models rely on image gradients for their energy functionals, making them effective for images with clear boundaries. For instance, Kass et al. [16] introduced the snake model, which uses internal energy for contour smoothness and external energy to drive the contour toward boundaries, but it requires the initial contour to be near the target and struggles with handling topological changes. Caselles et al. [4] addressed this issue with the geodesic active contour model, allowing contours to naturally split and merge, enabling the detection of multiple objects. On the other hand, region-based models use statistical information from image regions and often employ the level set method to minimize energy functionals. The typical global region-based models include the Mumford-Shah model [29], the Chan-Vese model [5], and the multi-phase model [37]. While effective for binary or multi-phase images, these models can struggle with intensity inhomogeneity due to their homogeneity assumption within each region. Afterward, to overcome this issue, many enhanced region-based methods have been developed to incorporate local statistical features into the energy functional, improving segmentation accuracy in such complex images [15,19,20,22,25,33,39,42–47].

With the additional help of prescribed marker points, variational selective segmentation models aim to extract specific objects by minimizing an energy functional that evaluates segmentation quality. This functional typically includes terms for data fidelity, contour length or smoothness, and other essential criteria, guiding the segmentation process to accurately capture the desired regions. Over time, variational selective segmentation models have evolved significantly. When the marker points were placed close to the boundary of the selected region, Gout et al. [9] combined the geodesic active contour [4] with a weighted Euclidean distance function using a level set approach. Badshah and Chen [2] enhanced this by incorporating intensity constraints from the Chan-Vese model [5], promoting the segmentation of homogeneous regions. Rada and Chen [31] further improved robustness with a two-level set method. However, these models often lacked size constraints for the detected objects, leading to over- or under-segmentation depending on the initialization. To address this issue, Rada and Chen [32] introduced area constraints, while Spencer and Chen [36] reformulated their model into a convex form using convex relaxation. More recently, Liu et al. [23] proposed a two-stage convex model that incorporates a distance function-dependent weight in the data-fitting term, allowing for a smooth approximation and utilizing a thresholding procedure to extract the

object of interest. Jumaat and Chen [14] reformulated the convex model in [36] through primal-dual formulation and introduced an optimization-based multilevel algorithm for the new model. Such an approach is less sensitive to the model parameters. A notable advance was made by Roberts et al. [34], who proposed a novel convex model using edge-weighted geodesic distance from a marker set as a penalty term, replacing the Euclidean distance. This geodesic distance was treated as a stand-alone fitting term, improving robustness and accuracy in complex images. However, the geodesic distance term must be computed using a PDE, requiring two additional tuning parameters.

In this paper, we propose a novel total variation (TV) distance-enhanced selective segmentation model for medical images, particularly those with intensity inhomogeneity. Building on the local intensity clustering (LIC) model from [18], we introduce an additional area constraint using a TV distance function to enhance selective segmentation accuracy. This novel distance function, derived from the simple single-scale Retinex [17,30] output image, measures the TV distance between points in image domain and prescribed marker points located within the target region. Such a simple yet unusual distance function has the property that the TV distance is close to zero for image points within the target region, while it approaches one for points outside that region. By incorporating this property as an area constraint, the TV distance function enables the segmentation contour to locate the selected objects correctly. Meanwhile, the other two terms in the model's energy functional−local intensity clustering energy and contour length regularization−work together to segment and tightly wrap the target objects accurately.

For the numerical implementation of the proposed model, we employ the efficient iterative convolution-thresholding (ICT) method [40, 41] to solve the energy minimization problem associated with the TV distance-enhanced selective segmentation model, rather than solving the associated Euler-Lagrange equation or further combined with the level set method which is computationally expensive due to the need to approximate solutions to partial differential equations. In contrast, the ICT method offers a more efficient, alternating-direction iterative approach, where each subproblem typically has a closed-form solution, greatly simplifying the computation. This method demonstrates versatility across a broad range of region-based segmentation models. A vital advantage of the ICT method is the guaranteed decay of the energy functional over iterations, ensuring convergence to a stationary partition. Finally, numerical experiments on medical images and comparisons with some well-known methods, such as that in [6,19,34,36,47], validate the effectiveness and efficiency of the proposed selective segmentation approach.

This paper makes two significant contributions. First, we introduce a novel TV distance function that considerably enhances the robustness and performance of the LIC fitting energy model [18]. This improvement allows for the more accurate segmentation of selected objects in medical images with intensity inhomogeneities. Second, by approximating the length of the segmentation contour through the convolution of a heat kernel with characteristic functions, we present an efficient ICT method for the numerical implementation of the proposed selective segmentation model, eliminating the need to solve PDEs. This method leads to energy decay at each iteration and promotes faster

convergence, as demonstrated by the numerical experiments and comparisons in Section 5.

The remainder of this paper is organized as follows. Section 2 introduces the novel TV distance function. Section 3 presents the TV distance-enhanced LIC model. Section 4 details the implementation of the model using the ICT method and includes a proof of the energy decay during the iterations. In Section 5, numerical experiments on some medical images are conducted. Finally, Section 6 provides a summary and conclusions.

2 The total variation distance function

Let $\Omega\subset\mathbb{R}^2$ be a bounded open rectangular domain with boundary $\partial\Omega$, and let $f:\overline{\Omega}\to\mathbb{R}_0^+$ represent a grayscale source image in $L^2(\Omega)$, intended for selective segmentation. Since we eventually want to segment digital images in a discrete domain, we can tacitly assume the differentiability of f without losing generality. We aim to perform a selective segmentation of f, focusing on extracting a specific region, denoted as Ω_1, based on the intensity distribution of f and aided by some prescribed marker points inside the target region Ω_1. Therefore, we assume that Ω is partitioned into two disjoint open regions Ω_i for $i=1,2$, and let $C=\partial\Omega_1\setminus\partial\Omega$ be the common boundary between them, excluding the parts that coincide with the overall domain boundary $\partial\Omega$. Thus, $\Omega=\Omega_1\cup C\cup\Omega_2$.

Let $M:=\{\boldsymbol{x}_1,\boldsymbol{x}_2,\cdots,\boldsymbol{x}_p\}$, where $p\geq 3$, denote the set of prescribed marker points with $\boldsymbol{x}_i\in\Omega_1$ for $1\leq i\leq p$. These marker points are not necessarily located near the boundary of Ω_1. We assume that they can be connected in an appropriate order to form a polygonal region. This resulting polygonal curve will serve as the initial segmentation contour introduced later in Section 4. Below we are going to define a simple distance function $d:\overline{\Omega}\to[0,1]$ such that as far as possible, $d(\boldsymbol{x})$ is near 0 for $\boldsymbol{x}\in\Omega_1$, while near 1 for $\boldsymbol{x}\in\Omega_2$. Given a point in the image domain, $\boldsymbol{x}\in\overline{\Omega}$ and $\boldsymbol{x}\neq\boldsymbol{x}_i$, we define the unit direction $\boldsymbol{n}_i$ by

$$\boldsymbol{n}_i=\frac{\boldsymbol{x}-\boldsymbol{x}_i}{\|\boldsymbol{x}-\boldsymbol{x}_i\|_2},\tag{2.1}$$

and the distance from the marker point $\boldsymbol{x}_i$ to $\boldsymbol{x}$ by the line integral along the edge $\overline{\boldsymbol{x}_i\boldsymbol{x}}$

$$t_i(\boldsymbol{x})=\int_{\overline{\boldsymbol{x}_i\boldsymbol{x}}}|\nabla f\cdot\boldsymbol{n}_i|ds.\tag{2.2}$$

Otherwise, if $\boldsymbol{x}$ is itself the marker point $\boldsymbol{x}_i$, then we define $t_i(\boldsymbol{x})=0$. See Fig. 1 for an illustration of the marker point $\boldsymbol{x}_i$ and unit direction $\boldsymbol{n}_i$.

Notice that the distance $t_i(\boldsymbol{x})$ is simply the integral of the absolute value of the directional derivative of f along the direction $\boldsymbol{n}_i$ from $\boldsymbol{x}_i$ to $\boldsymbol{x}$. It represents the 1-D total variation (TV) [1, 35] of f in the direction $\boldsymbol{n}_i$ on the line segment $\overline{\boldsymbol{x}_i\boldsymbol{x}}$. Intuitively, if $\overline{\boldsymbol{x}_i\boldsymbol{x}}$ crosses some edge of the image f, the magnitude of the gradient ∇f becomes large, causing the value of $t_i(\boldsymbol{x})$ to increase. Moreover, if $\overline{\boldsymbol{x}_i\boldsymbol{x}}$ crosses multiple edges in the image f, the value of $t_i(\boldsymbol{x})$ will increase even further. However, when $\boldsymbol{x}$ lies within the target region Ω_1, where the intensity of f is generally more homogeneous and varies only slightly,

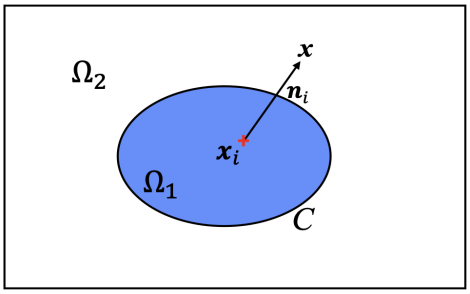

Figure 1: An illustration of the marker point x_i and unit direction n_i.

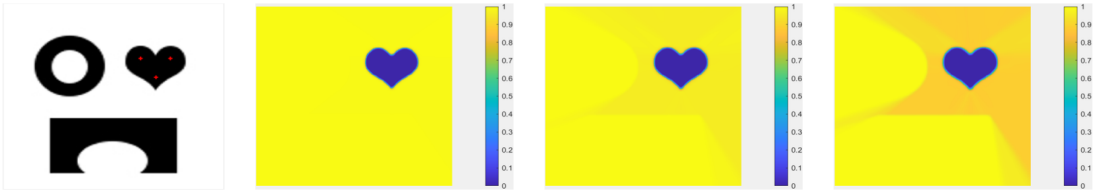

Figure 2: TV distance function d of a synthetic image f with intensity values in $[0,255]$ for different parameters: (a) source image f and three marker points x_i, denoted by symbol $+$ in red, where the black heart is the target region to be selected; (b), (c), and (d) are the computed results of $d(x)$ for $x\in\overline{\Omega}$ with $a=10\times255^2$, 15×255^2, and 20×255^2, respectively.

the magnitude of ∇f remains small along $\overline{x_i x}$, resulting in a small value for $t_i(x)$. If necessary, we may also use a pre-denoised image such as the convolution function $G_s * f$ to replace f in (2.2) when the source image f has a slight noise, where G_s is a properly truncated Gaussian kernel and $*$ denotes the convolution operation.

We now measure simultaneously the distances of the p marker points to the image domain point x and then define a normalized distance function $d:\overline{\Omega}\to[0,1]$ by

$$d(x):=\prod_{i=1}^{p}\left(1-\exp\left(-\frac{t_i^2(x)}{a}\right)\right), \tag{2.3}$$

where $a>0$ is a tuning parameter, and we call d the *TV distance function*. For an ideal grayscale image f shown in Fig. 2, we observe that $d(x)\approx0$ for $x\in\Omega_1$, whereas $d(x)\approx1$ for $x\in\Omega_2$, provided a is carefully chosen. This TV distance function will help the segmentation contour of the later proposed model to locate the selected objects initially. It is important to note that, generally speaking, the value $d(x)$ tends to be closer to 0 for $x\in\Omega_1$ when there are more marker points x_i in Ω_1. This occurs because each term on the right-hand side of equation (2.3) is significantly less than 1 for $x\in\Omega_1$. Consequently, the product of more terms that are each less than 1 is closer to 0.

It should be noted that intensity inhomogeneity inevitably occurs in real images from

various modalities. If the source image f exhibits intensity inhomogeneity, then the gradient ∇f may be affected and inconsistent when calculating t_i in (2.2), which could result in an improper TV distance function. To address this issue, we utilize the simple single-scale Retinex (SSR) model [17, 30] to produce a relatively more homogeneous image for accurately calculating the distances t_i. Broadly speaking, an SSR is part of the class of center/surround functions, where the output is determined by the difference between the center value and the average of its neighborhood. The general mathematical form of an SSR is given by

$$\widetilde{f}(\boldsymbol{x}) := \log\left(1+\frac{f(\boldsymbol{x})}{(G_r * f)(\boldsymbol{x})+\varepsilon}\right) \quad \text{for } \boldsymbol{x}\in\overline{\Omega}, \tag{2.4}$$

where G_r is a truncated Gaussian kernel, and $0<\varepsilon\ll 1$ is a small constant to prevent the denominator from becoming zero. Consequently, the definition of $t_i(\boldsymbol{x})$ in (2.2) will be modified as the line integral

$$t_i(\boldsymbol{x}) = \int_{\overline{\boldsymbol{x}_i\boldsymbol{x}}} |\nabla\widetilde{f}\cdot\boldsymbol{n}_i| ds, \quad 1\le i\le p. \tag{2.5}$$

The SSR output image $\widetilde{f}$ will alleviate the inconsistency for computing t_i and result in a more accurate TV distance function (2.3).

3 The proposed selective segmentation model

With the help of TV distance function (2.3), in this section, we propose our selective segmentation model. In this paper, we adopt characteristic functions to implicitly represent the segmentation contour. Let χ_i be the characteristic function defined in $\mathbb{R}^2$ whose support is the region Ω_i, given by

$$\chi_i(\boldsymbol{x}) = \begin{cases} 1, & \boldsymbol{x}\in\Omega_i \\ 0, & \boldsymbol{x}\in\mathbb{R}^2\setminus\Omega_i \end{cases} \quad \text{for } i=1,2 \quad \text{and} \quad \chi_1(\boldsymbol{x})+\chi_2(\boldsymbol{x})=1, \ \forall\, \boldsymbol{x}\in\Omega\setminus C. \tag{3.1}$$

The admissible set $\mathcal{S}$ for $\boldsymbol{\chi}=(\chi_1,\chi_2)$ is given by

$$\mathcal{S} = \Big\{\boldsymbol{\chi}\in(BV(\Omega))^2 : \chi_i(\boldsymbol{x})\in\{0,1\} \text{ for } i=1,2 \text{ and } \chi_1(\boldsymbol{x})+\chi_2(\boldsymbol{x})=1, \forall\, \boldsymbol{x}\in\Omega\setminus C\Big\}, \tag{3.2}$$

which is non-convex, and $BV(\Omega)$ denotes the bounded variation space [1].

Given a set of $p\ge 3$ marker points in the target region Ω_1, we propose a novel TV distance-enhanced selective segmentation model, which is formulated as the following energy minimization problem:

$$\min_{(b,\boldsymbol{c},\boldsymbol{\chi})\in L^2(\Omega)\times\mathbb{R}^2\times\mathcal{S}} \mathcal{E}(b,\boldsymbol{c},\boldsymbol{\chi}), \tag{3.3}$$

where the total energy functional $\mathcal{E}$ consists of three terms, defined as

$$\begin{aligned}\mathcal{E}(b,\boldsymbol{c},\boldsymbol{\chi}) :=& \theta\int_\Omega \chi_1(\boldsymbol{x})d(\boldsymbol{x})+\chi_2(\boldsymbol{x})\big(1-d(\boldsymbol{x})\big)d\boldsymbol{x}\\ &+\mu\sqrt{\frac{\pi}{\tau}}\int_\Omega \chi_1(\boldsymbol{x})(G_\tau * \chi_2)(\boldsymbol{x})d\boldsymbol{x}\\ &+\int_\Omega\Big(\sum_{i=1}^{2}\int_\Omega \chi_i(\boldsymbol{y})K_\rho(\boldsymbol{x}-\boldsymbol{y})\big(f(\boldsymbol{y})-b(\boldsymbol{x})c_i\big)^2 d\boldsymbol{y}\Big)d\boldsymbol{x},\end{aligned} \tag{3.4}$$

$\theta>0$ and $\mu>0$ are model parameters to modulate the three terms, f is the source image to be segmented, b is the bias field, $\boldsymbol{c}:=(c_1,c_2)\in\mathbb{R}^2$ is a constant vector, G_τ is a heat kernel function, $*$ is the convolution operation, and K_ρ is a truncated and normalized Gaussian kernel function. The last two terms in (3.4) essentially form the local intensity clustering energy functional, initially studied in [18] for global image segmentation of intensity-inhomogeneous images. However, we have modified the functional by introducing a new contour length estimate, $\int_\Omega \chi_1(\boldsymbol{x})(G_\tau*\chi_2)(\boldsymbol{x})d\boldsymbol{x}$, replacing the original computation of the contour length $|C|$ used in [18]. More importantly, we add an area constraint to the energy functional (3.4) as the first term, specifically for selective image segmentation. It is also important to note that information about the target region Ω_1 is already incorporated into the first term through the TV distance function d defined in (2.3).

In the following, we will sequentially explain the details of the three components in the total energy functional (3.4). The first term in (3.4) serves as an area constraint to correctly locate the selected objects. If the TV distance function d is perfectly estimated, we would have

$$d(\boldsymbol{x})=\begin{cases}0, & \boldsymbol{x}\in\Omega_1,\\ 1, & \boldsymbol{x}\in\Omega_2,\end{cases} \tag{3.5}$$

which implies that the integral, weighted by the model parameter $\theta>0$,

$$\theta\int_\Omega \chi_1(\boldsymbol{x})d(\boldsymbol{x})+\chi_2(\boldsymbol{x})\big(1-d(\boldsymbol{x})\big)d\boldsymbol{x} \tag{3.6}$$

would be equal to zero. However, in practice, we only achieve $0\le d(\boldsymbol{x})\ll 1$ for $\boldsymbol{x}\in\Omega_1$ and $0\ll d(\boldsymbol{x})\le 1$ for $\boldsymbol{x}\in\Omega_2$. Therefore, we aim to find χ_i, $i=1,2$, such that (3.6) is minimized.

The second term in (3.4) represents a contour length regularization. Using characteristic functions, we can approximate the length $|C|$ of the segmentation contour. Let $0<\tau\ll 1$ be a small constant, and define the heat kernel as

$$G_\tau(\boldsymbol{x})=\frac{1}{4\pi\tau}\exp\Big(-\frac{\|\boldsymbol{x}\|_2^2}{4\tau}\Big). \tag{3.7}$$

According to the results in [8,26], the length of the interface C separating Ω_1 from Ω_2 is related to the amount of heat escaping from Ω_2 into Ω_1. This can be further weighted by the model parameter μ and approximated as

$$\mu|C|\approx\mu\sqrt{\frac{\pi}{\tau}}\int_\Omega \chi_1(\boldsymbol{x})(G_\tau*\chi_2)(\boldsymbol{x})d\boldsymbol{x}. \tag{3.8}$$

By adjusting the parameter $\mu>0$, we request a tight wrapping around the target object.

The final term in (3.4) represents a local intensity fitting energy, derived from a local clustering criterion function and a bias assumption to address image intensity inhomogeneity. In imaging science, it is commonly assumed that the bias field accounts for intensity inhomogeneity, which is a frequent characteristic of medical images [12, 38]. In this paper, we consider the multiplicative bias model with additive noise,

$$f(\boldsymbol{x})=b(\boldsymbol{x})I(\boldsymbol{x})+n(\boldsymbol{x}),\quad \forall\,\boldsymbol{x}\in\overline{\Omega}, \tag{3.9}$$

where I is the true image, b is the bias field, and n is an additive zero-mean Gaussian noise, all are unknown except the source image f is given. Suppose that the true image I approximately takes two distinct constant values c_1 and c_2 in the disjoint regions Ω_1 and Ω_2, respectively. Since the bias field b is assumed to be a slowly varying function, for a given $\boldsymbol{x}\in\Omega$, we have

$$f(\boldsymbol{y})\approx b(\boldsymbol{x})c_i+n(\boldsymbol{y}),\quad \forall\,\boldsymbol{y}\in\mathcal{N}_\rho(\boldsymbol{x})\cap\Omega_i, \tag{3.10}$$

where $\mathcal{N}_\rho(\boldsymbol{x}):=\{\boldsymbol{y}\in\Omega:\|\boldsymbol{y}-\boldsymbol{x}\|_2\le\rho\}$ for a radius $\rho>0$. We introduce the nonnegative kernel function $K_\rho:\mathbb{R}^2\to\mathbb{R}_0^+$, which is a truncated and normalized Gaussian function,

$$K_\rho(\boldsymbol{z})=\begin{cases}\dfrac{1}{A}\exp\left(-\dfrac{\|\boldsymbol{z}\|_2^2}{2\sigma^2}\right), & \text{for } \|\boldsymbol{z}\|_2\le\rho,\\ 0, & \text{otherwise,}\end{cases} \tag{3.11}$$

where $A>0$ is a constant depending on ρ such that $\int_{\|\boldsymbol{z}\|_2\le\rho}K_\rho(\boldsymbol{z})d\boldsymbol{z}=1$, $\sigma>0$ is the standard deviation and $\rho>0$ is the effective radius of the Gaussian function usually depending on σ. Based on (3.9), Li et al. [18] introduced the local clustering criterion function,

$$E(\boldsymbol{x})=\sum_{i=1}^{2}\int_{\Omega_i}K_\rho(\boldsymbol{x}-\boldsymbol{y})\big(f(\boldsymbol{y})-b(\boldsymbol{x})c_i\big)^2d\boldsymbol{y}. \tag{3.12}$$

Then the smaller the value of $E(\boldsymbol{x})$, the better the classification of the local intensities $\{f(\boldsymbol{y}):\boldsymbol{y}\in\mathcal{N}_\rho(\boldsymbol{x})\}$. In [18], they defined the optimal partition $\{\Omega_1,\Omega_2\}$ of the entire domain Ω as the one such that the local clustering criterion function $E(\boldsymbol{x})$ is minimized for all $\boldsymbol{x}\in\Omega$. Thus, we consider the following local intensity clustering (LIC) fitting energy, which is the last term in the energy functional (3.4):

$$\int_\Omega\Big(\sum_{i=1}^{2}\int_\Omega\chi_i(\boldsymbol{y})K_\rho(\boldsymbol{x}-\boldsymbol{y})\big(f(\boldsymbol{y})-b(\boldsymbol{x})c_i\big)^2d\boldsymbol{y}\Big)d\boldsymbol{x}. \tag{3.13}$$

To sum up, by combining the three components (3.6), (3.8), and (3.13), we formulate the TV distance-enhanced total energy functional (3.4) for the proposed model (3.3). The energy functional (3.4) involves several parameters: θ, μ, τ, ρ, and σ. Generally, due to the continuity of the energy functional, the segmentation results are not highly sensitive to

these parameters. However, they must still be appropriately chosen based on the degree of intensity inhomogeneity, as each parameter has a distinct role. Specifically, θ adjusts the TV distance function term (3.6) to correctly locate the selected objects. The parameter μ governs the contour length; a larger μ is recommended when the object of interest is not tightly enclosed. A small value for τ in the heat kernel function (3.7) is sufficient to accurately approximate the contour length. Lastly, we set the effective radius $\rho:=2\sigma+h/2$ to control the local intensity fitting energy (3.13), where h is the grid size used in the Riemann sum for approximating the integrals on Ω (see Section 5). In general, a smaller ρ, which corresponds to a smaller standard deviation of the truncated and normalized Gaussian function (3.11), is used for images with higher intensity inhomogeneity.

4 The iterative convolution-thresholding method

In this section, we apply an efficient iterative convolution-thresholding (ICT) method to implement the proposed TV distance-enhanced selective segmentation model (3.3). The use of the ICT method for image segmentation was first studied by Wang et al. in [40,41]. This method provides an iterative solution framework that is well-suited for a variety of region-based segmentation models. Its primary advantage is the consistent decrease of total energy with each iteration, ensuring convergence to a stationary minimum regardless of the initial partition. Recently, this efficient method has been successfully adapted to other image segmentation models, as demonstrated in [13,21,22,24].

The ICT method for implementing the proposed selective segmentation model (3.3) can be divided into three steps. It works by alternating two convolution steps and one thresholding step. More specifically, suppose that we have the k-th iteration $b^{(k)}$, $\boldsymbol{c}^{(k)}$, and $\boldsymbol{\chi}^{(k)}$ for $k\geq 0$. Then, we seek $b^{(k+1)}\in L^2(\Omega)$, $\boldsymbol{c}^{(k+1)}\in\mathbb{R}^2$, and $\boldsymbol{\chi}^{(k+1)}\in\mathcal{S}$ sequentially satisfying the following three minimization subproblems:

$$b^{(k+1)}=\underset{b\in L^2(\Omega)}{\operatorname{argmin}}\mathcal{E}_1(b):=\mathcal{E}(b,\boldsymbol{c}^{(k)},\boldsymbol{\chi}^{(k)}), \tag{4.1}$$

$$\boldsymbol{c}^{(k+1)}=\underset{\boldsymbol{c}\in\mathbb{R}^n}{\operatorname{argmin}}\mathcal{E}_2(\boldsymbol{c}):=\mathcal{E}(b^{(k+1)},\boldsymbol{c},\boldsymbol{\chi}^{(k)}), \tag{4.2}$$

$$\boldsymbol{\chi}^{(k+1)}=\underset{\boldsymbol{\chi}\in\mathcal{S}}{\operatorname{argmin}}\mathcal{E}_3(\boldsymbol{\chi}):=\mathcal{E}(b^{(k+1)},\boldsymbol{c}^{(k+1)},\boldsymbol{\chi}). \tag{4.3}$$

We begin the b-subproblem (4.1) by observing that $\mathcal{E}_1(b)$ is a strictly convex functional in variable b. Setting the functional derivative $\delta\mathcal{E}_1/\delta b=0$, we have

$$\sum_{i=1}^{2}\int_\Omega \chi_i^{(k)}(\boldsymbol{y})K_\rho(\boldsymbol{x}-\boldsymbol{y})\big(f(\boldsymbol{y})-b(\boldsymbol{x})c_i^{(k)}\big)(-2c_i^{(k)})d\boldsymbol{y}=0, \tag{4.4}$$

which implies the bias field $b^{(k+1)}$ should be given by

$$b^{(k+1)}(\boldsymbol{x})=\frac{\big(K_\rho*\big(f\sum_{i=1}^2 c_i^{(k)}\chi_i^{(k)}\big)\big)(\boldsymbol{x})}{\big(K_\rho*\big(\sum_{i=1}^2(c_i^{(k)})^2\chi_i^{(k)}\big)\big)(\boldsymbol{x})}\quad\text{for }\boldsymbol{x}\in\Omega\backslash\mathcal{C}. \tag{4.5}$$

To solve the $\boldsymbol{c}$-subproblem (4.2), we set all the partial derivatives of $\mathcal{E}_2$ with respect to c_i to be zero, $\partial\mathcal{E}_2(\boldsymbol{c})/\partial c_i=0$. Then we obtain

$$-2\int_\Omega\int_\Omega \chi_i^{(k)}(\boldsymbol{y})K_\rho(\boldsymbol{x}-\boldsymbol{y})\big(f(\boldsymbol{y})-b^{(k+1)}(\boldsymbol{x})c_i\big)b^{(k+1)}(\boldsymbol{x})d\boldsymbol{y}d\boldsymbol{x}=0. \tag{4.6}$$

Since the truncated Gaussian function K_ρ in (3.11) is symmetric with respect to the origin, i.e., $K_\rho(\boldsymbol{x}-\boldsymbol{y})=K_\rho(\boldsymbol{y}-\boldsymbol{x})$, and we can exchange the order of integrations, it yields

$$\begin{aligned} &c_i\int_\Omega\int_\Omega \chi_i^{(k)}(\boldsymbol{y})\big(b^{(k+1)}(\boldsymbol{x})\big)^2K_\rho(\boldsymbol{y}-\boldsymbol{x})d\boldsymbol{x}d\boldsymbol{y}\\ &=\int_\Omega\int_\Omega \chi_i^{(k)}(\boldsymbol{y})f(\boldsymbol{y})b^{(k+1)}(\boldsymbol{x})K_\rho(\boldsymbol{y}-\boldsymbol{x})d\boldsymbol{x}d\boldsymbol{y}. \end{aligned} \tag{4.7}$$

Using the convolution notation, we gain the minimizer of subproblem (4.2),

$$c_i^{(k+1)}=\frac{\int_\Omega \chi_i^{(k)}(\boldsymbol{y})f(\boldsymbol{y})\big(b^{(k+1)}*K_\rho\big)(\boldsymbol{y})d\boldsymbol{y}}{\int_\Omega \chi_i^{(k)}(\boldsymbol{y})\big((b^{(k+1)})^2*K_\rho\big)(\boldsymbol{y})d\boldsymbol{y}}\quad\text{for } i=1,2. \tag{4.8}$$

To address the $\boldsymbol{\chi}$-subproblem (4.3), we note that it is not a convex minimization problem, since the admissible set $\mathcal{S}$ of characteristic functions defined in (3.2) is not a convex set. For linearizing the energy functional $\mathcal{E}_3(\boldsymbol{\chi})$ at $\boldsymbol{\chi}^{(k)}$ in a convex set that will be used later, we directly introduce the convex hull $\mathcal{K}$ of $\mathcal{S}$,

$$\mathcal{K}=\Big\{\boldsymbol{\chi}\in(BV(\Omega))^2:0\le\chi_i(\boldsymbol{x})\le1 \text{ for } i=1,2 \text{ and } \chi_1(\boldsymbol{x})+\chi_2(\boldsymbol{x})=1,\ \forall\boldsymbol{x}\in\Omega\backslash\mathcal{C}\Big\}, \tag{4.9}$$

and then consider the equivalent minimization problem instead:

$$\boldsymbol{\chi}^{(k+1)}=\operatorname*{argmin}_{\boldsymbol{\chi}\in\mathcal{K}}\mathcal{E}_3(\boldsymbol{\chi}). \tag{4.10}$$

The equivalence between (4.3) and (4.10) holds because the energy functional $\mathcal{E}_3(\boldsymbol{\chi})$ is strictly concave with respect to $\boldsymbol{\chi}$ over the convex hull $\mathcal{K}$. As a result, the minimizer must lie on the boundary of the convex set $\mathcal{K}$, which corresponds to the subset $\mathcal{S}$. This conclusion is formalized in the following proposition. The detailed proof follows a similar argument in [21] (see also [41]), with minor modifications, and is thus omitted.

Proposition 4.1. *The energy functional $\mathcal{E}_3$ defined in* (4.3) *is strictly concave in $\boldsymbol{\chi}$ over the convex set $\mathcal{K}$, which implies that*

$$\operatorname*{argmin}_{\boldsymbol{\chi}\in\mathcal{S}}\mathcal{E}_3(\boldsymbol{\chi})=\operatorname*{argmin}_{\boldsymbol{\chi}\in\mathcal{K}}\mathcal{E}_3(\boldsymbol{\chi}). \tag{4.11}$$

Now, linearizing the energy functional $\mathcal{E}_3(\boldsymbol{\chi})$ at $\boldsymbol{\chi}^{(k)}$ in the convex hull $\mathcal{K}$, we obtain

$$\mathcal{E}_3(\boldsymbol{\chi})\approx\mathcal{E}_3(\boldsymbol{\chi}^{(k)})+\sum_{i=1}^2\int_\Omega\frac{\delta\mathcal{E}_3}{\delta\chi_i}\bigg|_{\boldsymbol{\chi}=\boldsymbol{\chi}^{(k)}}\Big(\chi_i(\boldsymbol{x})-\chi_i^{(k)}(\boldsymbol{x})\Big)d\boldsymbol{x}=:\widetilde{\mathcal{E}}_3(\boldsymbol{\chi}), \tag{4.12}$$

where we define the linearized functional in (4.12) as $\widetilde{\mathcal{E}}_3(\boldsymbol{\chi})$. Then

$$\widetilde{\mathcal{E}}_3(\boldsymbol{\chi}) := \mathcal{E}_3(\boldsymbol{\chi}^{(k)}) + \sum_{i=1}^{2} \int_\Omega \varphi_i^{(k)}(\boldsymbol{x}) \left(\chi_i(\boldsymbol{x}) - \chi_i^{(k)}(\boldsymbol{x})\right) d\boldsymbol{x}, \tag{4.13}$$

where the function $\varphi_i^{(k)}$ is given by

$$\begin{aligned}\varphi_i^{(k)}(\boldsymbol{x}) := \frac{\delta \mathcal{E}_3}{\delta \chi_i}(\boldsymbol{\chi}^{(k)}) &= \theta w_i(\boldsymbol{x}) + \mu \sqrt{\frac{\pi}{\tau}} \sum_{j=1, j\neq i}^{2} (G_\tau * \chi_j^{(k)})(\boldsymbol{x}) \\ &\quad + \int_\Omega K_\rho(\boldsymbol{y}-\boldsymbol{x}) \left(f(\boldsymbol{x}) - b^{(k+1)}(\boldsymbol{y}) c_i^{(k+1)}\right)^2 d\boldsymbol{y} \geq 0,\end{aligned} \tag{4.14}$$

and

$$w_1(\boldsymbol{x}) := d(\boldsymbol{x}) \quad \text{and} \quad w_2(\boldsymbol{x}) := 1 - d(\boldsymbol{x}). \tag{4.15}$$

Dropping the constant terms on the right-hand side of (4.13), we approximate the minimization problem (4.10) by

$$\widetilde{\boldsymbol{\chi}}^{(k+1)} = \underset{\boldsymbol{\chi}\in\mathcal{K}}{\operatorname{argmin}} \widetilde{\mathcal{E}}_3(\boldsymbol{\chi}) = \underset{\boldsymbol{\chi}\in\mathcal{K}}{\operatorname{argmin}} \sum_{i=1}^{2} \int_\Omega \varphi_i^{(k)}(\boldsymbol{x}) \chi_i(\boldsymbol{x}) d\boldsymbol{x}. \tag{4.16}$$

That is, we obtain a convex optimization problem of a linear functional in $\boldsymbol{\chi}$ over the convex hull $\mathcal{K}$. According to (4.14) and (3.1), we have $\varphi_i^{(k)}(\boldsymbol{x}) \geq 0$ and $\chi_i(\boldsymbol{x}) \geq 0$ for all $\boldsymbol{x} \in \Omega$, and then one of the minimizers of problem (4.16) can be easily attained,

$$\widetilde{\chi}_i^{(k+1)}(\boldsymbol{x}) = \begin{cases} 1, & \text{if } \varphi_i^{(k)}(\boldsymbol{x}) = \min\limits_{1\leq \ell \leq 2} \varphi_\ell^{(k)}(\boldsymbol{x}), \\ 0, & \text{otherwise,} \end{cases} \quad \text{for } i = 1,2. \tag{4.17}$$

Thus we assign

$$\boldsymbol{\chi}^{(k+1)}(\boldsymbol{x}) := \widetilde{\boldsymbol{\chi}}^{(k+1)}(\boldsymbol{x}) \tag{4.18}$$

as an approximate solution to the $\boldsymbol{\chi}$-subproblem (4.3).

In summary, the ICT method is divided into three steps. The first two convolution steps find $b^{(k+1)}$ by (4.5) and $\boldsymbol{c}^{(k+1)}$ by (4.8), respectively. The last thresholding step defines $\boldsymbol{\chi}^{(k+1)}$ via (4.18). The algorithm of the ICT method is described in Algorithm 1, where we use a sufficient small L^2-norm of the difference between two successive characteristic functions as the stopping criterion.

Remark 4.1. Assume that the grayscale digital image f to be segmented has dimensions $m \times n$, and let $N := mn$. The computational complexity of each iteration in Algorithm 1 can be readily estimated. Both the convolution steps for computing b in (4.5) and $\boldsymbol{c}$ in (4.8) require $\mathcal{O}(N \log N)$ operations when implemented using the fast Fourier transform (FFT). Likewise, the computation of $\varphi_i^{(k)}$ in the thresholding step for $\boldsymbol{\chi}$ in (4.17) also has a complexity of $\mathcal{O}(N \log N)$. Thus, the overall complexity per iteration of the ICT method is $\mathcal{O}(N \log N)$.

Algorithm 1 : ICT method for solving the proposed model (3.3)

input: $b^{(0)}$, $\boldsymbol{c}^{(0)}$, and $\boldsymbol{\chi}^{(0)}$; $tolerance>0$; $error\gg tol$.
while $error\geq tolerance$: do
  convolution step for b: find the function $b^{(k+1)}$ by (4.5)
  convolution step for $\boldsymbol{c}$: find the constant vector $\boldsymbol{c}^{(k+1)}$ by (4.8)
  thresholding step for $\boldsymbol{\chi}$: update the characteristic function $\boldsymbol{\chi}^{(k+1)}$ by (4.18)
  update $error=\|\boldsymbol{\chi}^{(k+1)}-\boldsymbol{\chi}^{(k)}\|_{(L^2(\Omega))^2}$ and advance the counter $k\leftarrow k+1$
end while
output: $b^{(k)}$, $\boldsymbol{c}^{(k)}$, and $\boldsymbol{\chi}^{(k)}$.

Next, we show that the total energy functional (3.4) of the proposed model (3.3) decays in the ICT method, which ensures convergence for any initialization.

Theorem 4.1. *The energy functional* (3.4) *of the proposed model* (3.3) *decays in the ICT method in the following way:*

$$\mathcal{E}(b^{(k+1)},\boldsymbol{c}^{(k+1)},\boldsymbol{\chi}^{(k+1)})\leq\mathcal{E}(b^{(k)},\boldsymbol{c}^{(k)},\boldsymbol{\chi}^{(k)}),\quad\forall\,k\geq 0. \tag{4.19}$$

Proof. From (4.2) and (4.1), we immediately have

$$\mathcal{E}(b^{(k+1)},\boldsymbol{c}^{(k+1)},\boldsymbol{\chi}^{(k)})\leq\mathcal{E}(b^{(k+1)},\boldsymbol{c}^{(k)},\boldsymbol{\chi}^{(k)})\leq\mathcal{E}(b^{(k)},\boldsymbol{c}^{(k)},\boldsymbol{\chi}^{(k)}). \tag{4.20}$$

Since $\mathcal{E}_3(\boldsymbol{\chi}):=\mathcal{E}(b^{(k+1)},\boldsymbol{c}^{(k+1)},\boldsymbol{\chi})$, we only need to prove

$$\mathcal{E}_3(\boldsymbol{\chi}^{(k+1)})\leq\mathcal{E}_3(\boldsymbol{\chi}^{(k)}), \tag{4.21}$$

which is non-trivial because we assign $\boldsymbol{\chi}^{(k+1)}(\boldsymbol{x}):=\widetilde{\boldsymbol{\chi}}^{(k+1)}(\boldsymbol{x})$ in (4.18) and $\widetilde{\boldsymbol{\chi}}^{(k+1)}(\boldsymbol{x})$ defined in (4.17) is a minimizer of the linearized minimization problem (4.16), only having

$$\widetilde{\mathcal{E}}_3(\boldsymbol{\chi}^{(k+1)})\leq\widetilde{\mathcal{E}}_3(\boldsymbol{\chi}^{(k)})=\mathcal{E}_3(\boldsymbol{\chi}^{(k)}). \tag{4.22}$$

Through straightforward calculation, we have

$$\begin{aligned}
&\mathcal{E}_3(\boldsymbol{\chi}^{(k+1)})-\mathcal{E}_3(\boldsymbol{\chi}^{(k)})\\
=&\theta\int_\Omega d(\boldsymbol{x})\Big(\chi_1^{(k+1)}(\boldsymbol{x})-\chi_1^{(k)}(\boldsymbol{x})\Big)+(1-d(\boldsymbol{x}))\Big(\chi_2^{(k+1)}(\boldsymbol{x})-\chi_2^{(k)}(\boldsymbol{x})\Big)d\boldsymbol{x}\\
&+\mu\sqrt{\frac{\pi}{\tau}}\int_\Omega\Big(\chi_1^{(k+1)}(\boldsymbol{x})(G_\tau*\chi_2^{(k+1)})(\boldsymbol{x})-\chi_1^{(k)}(\boldsymbol{x})(G_\tau*\chi_2^{(k)})(\boldsymbol{x})\Big)d\boldsymbol{x}\\
&+\int_\Omega\Big(\sum_{i=1}^2\int_\Omega\Big(\chi_i^{(k+1)}(\boldsymbol{y})-\chi_i^{(k)}(\boldsymbol{y})\Big)K_\rho(\boldsymbol{x}-\boldsymbol{y})\big(f(\boldsymbol{y})-b^{(k+1)}(\boldsymbol{x})c_i^{(k+1)}\big)^2d\boldsymbol{y}\Big)d\boldsymbol{x}.
\end{aligned}\tag{4.23}$$

From (4.16) and (4.18), we have the inequality

$$\sum_{i=1}^2\int_\Omega\varphi_i^{(k)}(\boldsymbol{x})\chi_i^{(k+1)}(\boldsymbol{x})d\boldsymbol{x}\leq\sum_{i=1}^2\int_\Omega\varphi_i^{(k)}(\boldsymbol{x})\chi_i^{(k)}(\boldsymbol{x})d\boldsymbol{x}, \tag{4.24}$$

which, combined with (4.14) and (4.23), leads to

$$\begin{aligned}
&\mathcal{E}_3(\boldsymbol{\chi}^{(k+1)})-\mathcal{E}_3(\boldsymbol{\chi}^{(k)})\\
\leq&\mu\sqrt{\frac{\pi}{\tau}}\int_\Omega\Big(\chi_1^{(k+1)}(\boldsymbol{x})(G_\tau*\chi_2^{(k+1)})(\boldsymbol{x})-\chi_1^{(k)}(\boldsymbol{x})(G_\tau*\chi_2^{(k)})(\boldsymbol{x})\Big)d\boldsymbol{x}\\
&-\mu\sqrt{\frac{\pi}{\tau}}\int_\Omega\Big(\chi_1^{(k+1)}(\boldsymbol{x})-\chi_1^{(k)}(\boldsymbol{x})\Big)(G_\tau*\chi_2^{(k)})(\boldsymbol{x})d\boldsymbol{x}\\
&-\mu\sqrt{\frac{\pi}{\tau}}\int_\Omega\Big(\chi_2^{(k+1)}(\boldsymbol{x})-\chi_2^{(k)}(\boldsymbol{x})\Big)(G_\tau*\chi_1^{(k)})(\boldsymbol{x})d\boldsymbol{x}.
\end{aligned}\tag{4.25}$$

Notice that the heat kernel G_τ defined in (3.7) satisfies the property,

$$G_{\tau_1+\tau_2}(\boldsymbol{x})=(G_{\tau_1}*G_{\tau_2})(\boldsymbol{x}),\quad\forall\ \tau_1,\tau_2>0,\tag{4.26}$$

and for $\chi,\psi\in BV(\Omega)$ with $\chi(\boldsymbol{x})=0$ and $\psi(\boldsymbol{x})=0$ for $\boldsymbol{x}\in\mathbb{R}^2\setminus\Omega$, we have

$$\int_\Omega\chi(\boldsymbol{x})(G_\tau*\psi)(\boldsymbol{x})d\boldsymbol{x}=\int_\Omega(G_{\tau/2}*\chi)(\boldsymbol{y})(G_{\tau/2}*\psi)(\boldsymbol{y})d\boldsymbol{y}=\int_\Omega\psi(\boldsymbol{x})(G_\tau*\chi)(\boldsymbol{x})d\boldsymbol{x}.\tag{4.27}$$

From (4.25) with (4.26), (4.27), and the fact that $\chi_2^{(k)}(\boldsymbol{x})=1-\chi_1^{(k)}(\boldsymbol{x})$ for all $k\in\mathbb{N}$ and $\boldsymbol{x}\in\Omega\setminus C$, we obtain

$$\begin{aligned}
&\mathcal{E}_3(\boldsymbol{\chi}^{(k+1)})-\mathcal{E}_3(\boldsymbol{\chi}^{(k)})\\
\leq&\mu\sqrt{\frac{\pi}{\tau}}\int_\Omega\Big(\chi_2^{(k+1)}(\boldsymbol{x})-\chi_2^{(k)}(\boldsymbol{x})\Big)\Big(G_\tau*\big(\chi_1^{(k+1)}-\chi_1^{(k)}\big)\Big)(\boldsymbol{x})d\boldsymbol{x}\\
=&\mu\sqrt{\frac{\pi}{\tau}}\int_\Omega\Big(1-\chi_1^{(k+1)}(\boldsymbol{x})-1+\chi_1^{(k)}(\boldsymbol{x})\Big)\Big(G_\tau*\big(\chi_1^{(k+1)}-\chi_1^{(k)}\big)\Big)(\boldsymbol{x})d\boldsymbol{x}\\
=&-\mu\sqrt{\frac{\pi}{\tau}}\int_\Omega\Big(\chi_1^{(k+1)}(\boldsymbol{x})-\chi_1^{(k)}(\boldsymbol{x})\Big)\Big(G_\tau*\big(\chi_1^{(k+1)}-\chi_1^{(k)}\big)\Big)(\boldsymbol{x})d\boldsymbol{x}\\
=&-\mu\sqrt{\frac{\pi}{\tau}}\int_\Omega\Big(\big(G_{\tau/2}*(\chi_1^{(k+1)}-\chi_1^{(k)})\big)(\boldsymbol{x})\Big)^2d\boldsymbol{x}\leq 0.
\end{aligned}$$

This completes the proof. □

5 Numerical experiments

In this section, we present numerical experiments and comparisons to assess the performance of the proposed TV distance-enhanced selective segmentation model (3.3), implemented using the ICT method on several medical images, particularly those with intensity inhomogeneity. All computations are performed on a laptop with a 13th Gen Intel Core i7-1360P processor and 16 GB of RAM. Consider a grayscale digital image f with

dimensions $m\times n$, where pixel values range from 0 to 255. The image f can be treated as a nonnegative piecewise constant function defined on the domain $\overline{\Omega}:=[0,mh]\times[0,nh]$, consisting of $m\times n$ squares with a small side length h. The integrals over Ω in the ICT Algorithm 1 are approximated by Riemann sums. In the following, model parameters are denoted by $\widetilde{\mu}$, $\widetilde{\theta}$, $\widetilde{\sigma}$, $\widetilde{\rho}$, and $\widetilde{\tau}$, defined as $\mu=\widetilde{\mu}h$, $\theta=\widetilde{\theta}h$, $\sigma=\widetilde{\sigma}h$, $\rho=\widetilde{\rho}h$, and $\tau=\widetilde{\tau}h^2$. Unless otherwise specified, the radius ρ of the truncated and normalized Gaussian function K_ρ is set as $\rho=2\sigma+h/2$, where σ is its standard deviation. In the discrete case, the Gaussian filter is represented as a $(2\widetilde{\rho})\times(2\widetilde{\rho})$ symmetric matrix.

In the following numerical simulations, each image contains $p\geq 3$ marker points, indicated by red $+$ symbols. The initial characteristic function $\boldsymbol{\chi}^{(0)}=(\chi_1^{(0)},\chi_2^{(0)})$ is constructed by setting $\chi_1^{(0)}(\boldsymbol{x})=1$ for all $\boldsymbol{x}$ inside the polygonal region enclosed by the curve formed by directly connecting these marker points, and $\chi_1^{(0)}(\boldsymbol{x})=0$ elsewhere. The complementary function is then defined as $\chi_2^{(0)}(\boldsymbol{x}):=1-\chi_1^{(0)}(\boldsymbol{x})$ for all $\boldsymbol{x}\in\overline{\Omega}$. In the first four examples, where the medical images exhibit slight intensity inhomogeneity, the TV distance function d is calculated using (2.2) and (2.3). For the fifth example, which involves more pronounced intensity inhomogeneity, we compute the TV distance function d using (2.5) and (2.3).

Example 5.1 (Selection of model parameters)**.** We begin by examining the role of the parameter $a>0$ in the TV distance function (2.3) for a 256×256 knee joint MRI image labeled as Image1 (see Fig. 3) with $p=3$ marker points, where the intensity values lie in the range $[0,255]$. We perform pre-denoising on the image using a simple 3×3 Gaussian filter and then test several parameter values, namely $a=(5,10,15,20,25,30,35)\times255^2$, and display the resulting TV distance functions in Fig. 3. From the numerical results, we observe that when a is too small, such as $a=5\times255^2$, the function $d(\boldsymbol{x})$ does not approximate zero over a significant portion of Ω_1. On the other hand, when a is too large, such as $a=35\times255^2$, the value of $d(\boldsymbol{x})$ may fail to approach one for points $\boldsymbol{x}$ in Ω_2 near the boundary of Ω_1. Therefore, the parameter a should be chosen appropriately to represent the TV distance function d accurately. We choose $a=25\times255^2$ as a balanced and effective value in the following numerical simulations.

Since a small value of the parameter in the heat kernel function (3.7) is sufficient to approximate the contour length accurately, we set $\widetilde{\tau}=2$. For the MRI image of the knee joint shown in Fig. 3, which exhibits slight intensity inhomogeneity, a slightly larger effective radius for the Gaussian function (3.11) is appropriate. Therefore, we choose $\widetilde{\rho}=16.5$. We now examine the model parameters $\widetilde{\theta}=(0.03,0.05,0.07,0.09)\times255^2$ and $\widetilde{\mu}=(0.03,0.05,0.07,0.09)\times255^2$, resulting in a total of sixteen parameter combinations. With the three marker points and initial contour indicated in Fig. 3, the corresponding selective segmentation results of the proposed method are presented in Fig. 4. From the numerical results reported in Fig. 4, we observe that when either $\widetilde{\theta}$ or $\widetilde{\mu}$ is too small, the proposed method fails to produce accurate segmentation. Consequently, in all subsequent numerical experiments, we adopt $\widetilde{\theta}=0.07\times255^2$ and $\widetilde{\mu}=0.05\times255^2$.

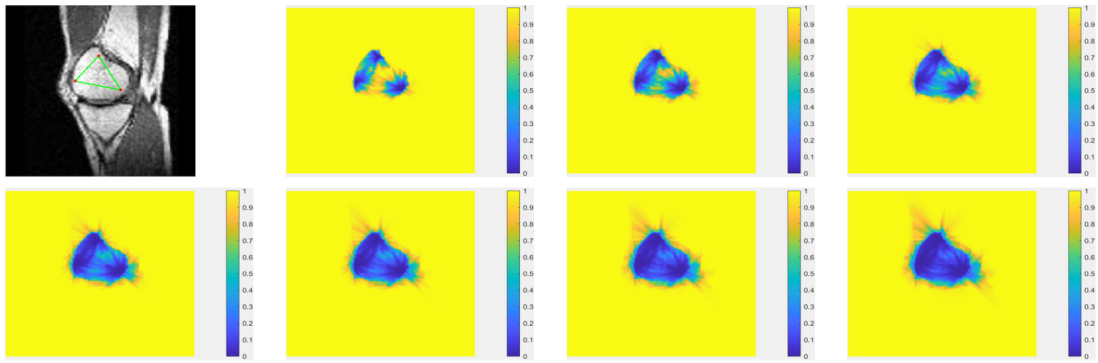

Figure 3: (Example 5.1) TV distance function d with different parameter values $a=(5,10,15,20,25,30,35)\times 255^2$ from left to right and top to bottom.

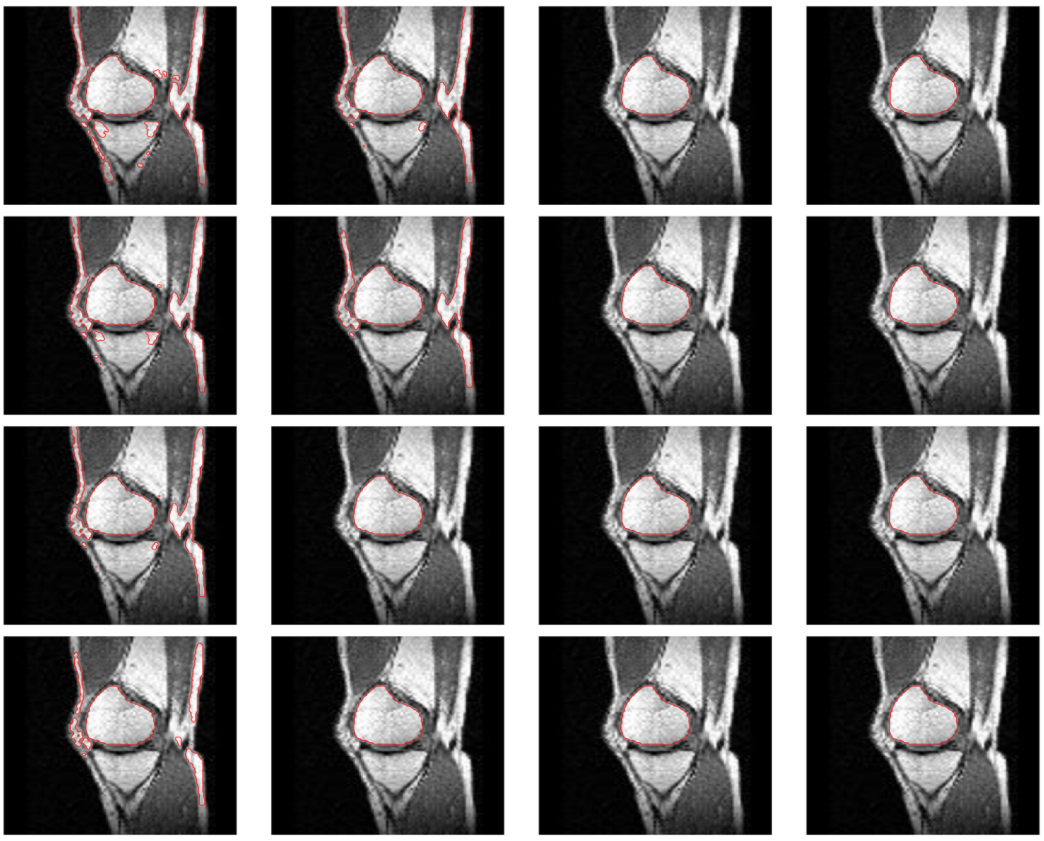

Figure 4: (Example 5.1) The selective segmentation results of the proposed method for different parameter values from left to right: First row: $\widetilde{\theta}=0.03\times 255^2$ and $\widetilde{\mu}=(0.03,0.05,0.07,0.09)\times 255^2$; Second row: $\widetilde{\theta}=0.05\times 255^2$ and $\widetilde{\mu}=(0.03,0.05,0.07,0.09)\times 255^2$; Third row: $\widetilde{\theta}=0.07\times 255^2$ and $\widetilde{\mu}=(0.03,0.05,0.07,0.09)\times 255^2$; Fourth row: $\widetilde{\theta}=0.09\times 255^2$ and $\widetilde{\mu}=(0.03,0.05,0.07,0.09)\times 255^2$.

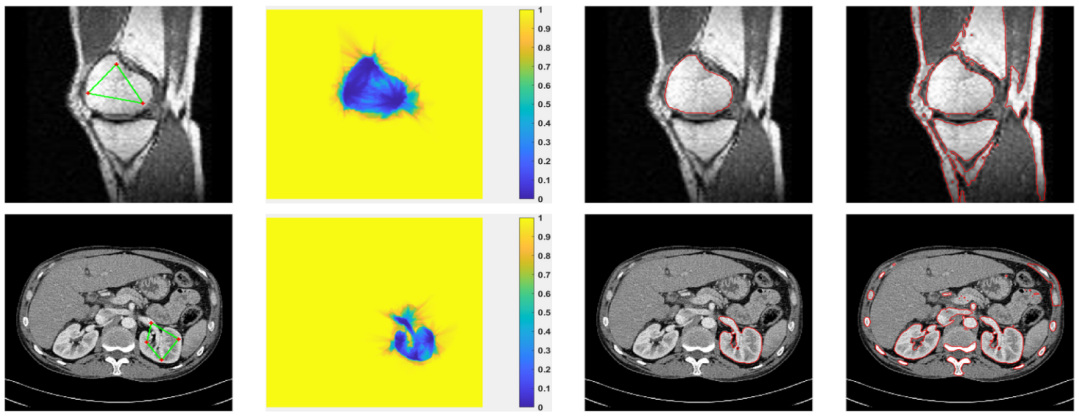

Figure 5: (Example 5.2) Verification of the significance of the area constraint term: (a) source image f with marker points and initial characteristic function $\chi^{(0)}$; (b) TV distance function d; (c) segmentation results by the proposed model (3.3); (d) segmentation results by the LIC model [18] (i.e., the proposed model with $\theta=0$).

Example 5.2 (Significance of the area constraint term)**.** To confirm the importance of the area constraint term–namely, the first term in (3.4)–within the proposed model (3.3), we conduct tests on Image1 in Example 5.1 with an additional 256×256 abdominal CT image (labeled as Image3). This area constraint primarily ensures the correct enclosure of the target object. When this term is omitted, i.e., $\theta=0$, the model reduces to the classical LIC model studied in [18], designed for global image segmentation. The numerical results are shown in Fig. 5, where these two images have been slightly pre-denoised using a simple 3×3 Gaussian filter. The parameters of the proposed model for both images are specified as $\widetilde{\theta}=0.07\times255^2$, $\widetilde{\mu}=0.05\times255^2$, $a=25\times255^2$, $\widetilde{\tau}=2$, and $\widetilde{\rho}=16.5$ as in Example 5.1. For the LIC model ($\theta=0$), we carefully tune the parameter $\widetilde{\mu}$ to achieve optimal results, including respective values such as $\widetilde{\mu}=0.002\times255^2$ and 0.04×255^2 for these two images. As illustrated in Fig. 5, without the area constraint term, the global segmentation model tends to isolate all foreground objects. By contrast, the proposed model (3.3) correctly segments the target region guided by the prescribed marker points, highlighting the critical role of the area constraint term.

Example 5.3 (Robustness of the proposed model)**.** Using the Image1 in Example 5.1 as a test image, we investigate the robustness of the proposed model (3.3) to the number and positions of marker points, $\boldsymbol{x}_i\in\Omega_1$ for $1\le i\le p$ and $p\ge3$, on the segmentation accuracy. The parameters in this example are specified as $\widetilde{\theta}=0.07\times255^2$, $\widetilde{\mu}=0.05\times255^2$, $a=25\times255^2$, $\widetilde{\tau}=2$, and $\widetilde{\rho}=16.5$ for all cases as that in Example 5.1. First, we randomly select distinct marker points within the target region Ω_1 for $p=3,4,5,6$, as shown in Fig. 6 along with the initial segmentation contours. For each p, the corresponding TV distance function d is also plotted in Fig. 6. As mentioned in Section 2, the value of $d(\boldsymbol{x})$ for $\boldsymbol{x}\in\Omega_1$

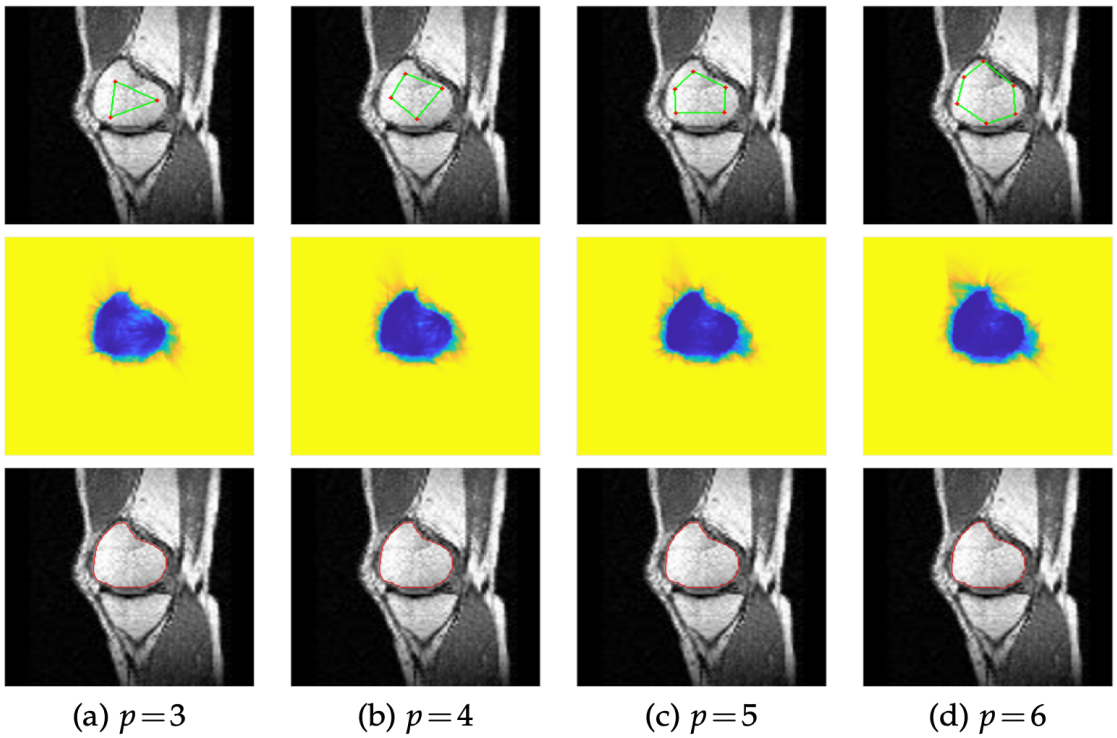

Figure 6: (Example 5.3) The selective segmentation results of Image1 using the proposed method for different number of marker points: $p=3,4,5,6$. The second row displays the corresponding TV distance function d. The iteration numbers of the ICT method for cases (a), (b), (c), and (d) are 22, 18, 14, and 11, respectively.

generally tends to be closer to 0 when more marker points are placed in Ω_1. In other words, increasing the number of marker points p tends to enhance the accuracy of the TV distance function d. Consequently, when we consider the first term in the model's energy functional (3.4), it intuitively accelerates the convergence of the segmentation process. This observation is supported by the results in Fig. 6.

Next, we examine the impact of marker point positions by considering eight cases. In each case, we randomly select three marker points (i.e., $p=3$) within the target region Ω_1 and construct the initial segmentation contour by connecting these points. The segmentation results conducted by the proposed model (3.3) are shown in Fig. 7, where we also record the iteration numbers of the ICT method for all cases. These results indicate that the positions of the marker points do not significantly affect the segmentation outcome. This property differs from typical global segmentation models, in which the final segmentation is often highly dependent on the initial contour. This difference may be because we have incorporated an area constraint in our selective segmentation model (3.3). This constraint ensures the initial contour grows confined within the target region Ω_1, and the initial contour is generally not far from the boundary of the desired target region.

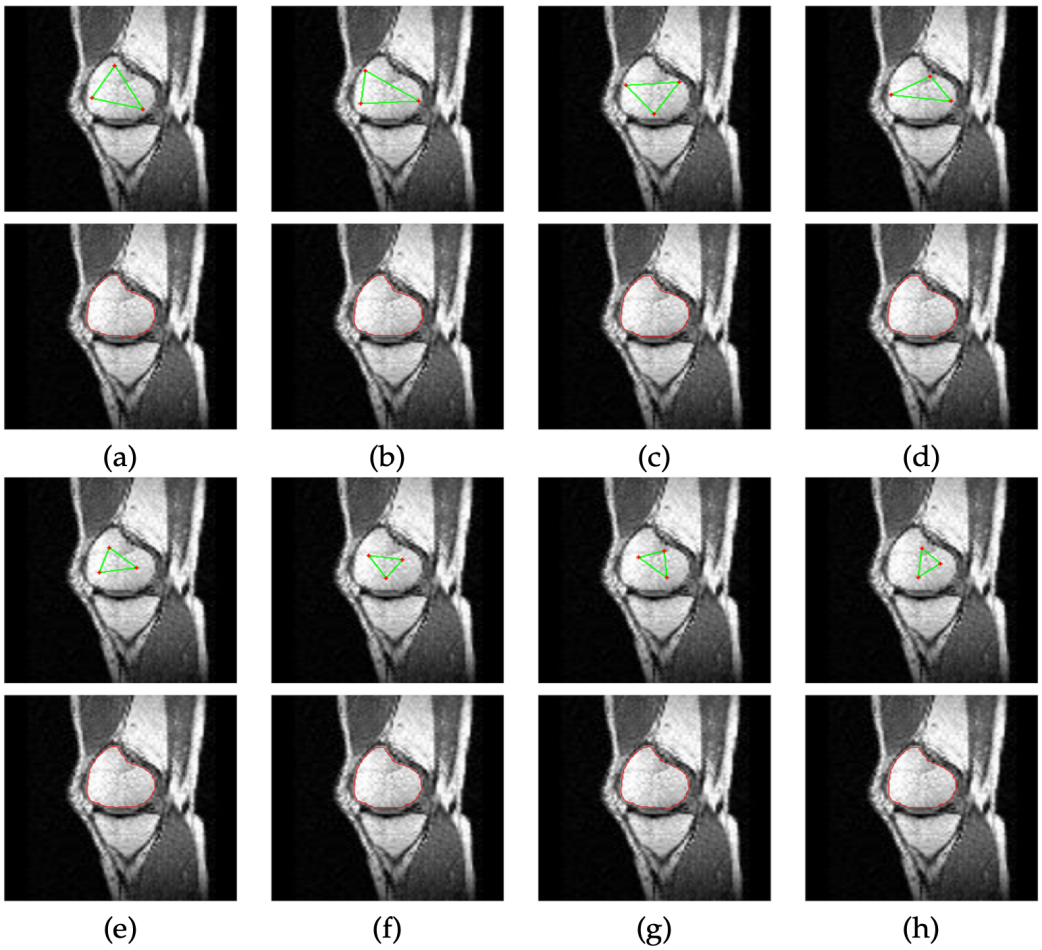

Figure 7: (Example 5.3) The selective segmentation results for Image1 using the proposed method for $p=3$ with eight different marker point positions and initial characteristic functions. The iteration numbers of the ICT method for cases from (a) to (h) are 23, 29, 27, 21, 25, 25, 29, and 26, respectively.

Example 5.4 (Test images with slight intensity inhomogeneity)**.** In this example, we evaluate the performance of the proposed model (3.3), implemented via the ICT method, on six 256×256 medical images (labeled Image1 through Image6) with slight intensity inhomogeneity. Fig. 8 displays the selective segmentation results, along with plots of the TV distance function d and the energy decay over ICT iterations. For all images, the model parameters are set the same as in Example 5.1, except for Image6, where we take $\widetilde{\theta}=0.08\times255^2$, $\widetilde{\mu}=0.09\times255^2$, and $a=5\times255^2$ to improve accuracy. The adjustment of model parameters for Image6 is necessary because the distance $t_i(\boldsymbol{x})$ from the marker point $\boldsymbol{x}_i$ to the image points $\boldsymbol{x}$ within the left-hand area of the target region is relatively small. Consequently, if we set $a=25\times255^2$, same as that for other images, the resulting TV distance function d creates an overly large and dispersed enclosure, which does not

accurately locate the target region at the outset. From the numerical results depicted in Fig. 8, we confirm the effectiveness and efficiency of the proposed selective image segmentation approach. Notably, the ICT method achieves convergence within 18 iterations across all test medical images.

Example 5.5 (Comparison of different models for images with significant intensity inhomogeneity)**.** In this example, we compare the proposed model (3.3) with several well-established models for segmenting Image1-Image6 with stronger intensity inhomogeneity. The models considered include the Spencer-Chen (SC) model [36], the Roberts-Chen-Irion (RCI) model [34], the piecewise-quadratic Mumford-Shah (PQMS) model [6], the local binary fitting (LBF) energy model [19], and the local statistical fitting (LSF) energy model [47]. Notably, the first two models, SC and RCI, are selective segmentation models whose numerical implementations are based on computer codes available on Chen's website: `https://www.liverpool.ac.uk/~cmchenke/`, where the associated Euler-Lagrange PDE is solved via an additive operator splitting algorithm [36]. In contrast, the latter three models–PQMS, LBF, and LSF–are region-based models designed for global segmentation and are implemented using efficient ICT methods similar to those introduced in Section 4.

In practical implementations, we carefully adjust the model parameters and initialization for all models to achieve the best possible results. For the three global segmentation models–PQMS, LBF, and LSF–we ensure that the initial contours are positioned close to the boundaries of the target region. Fig. 9 presents the comparison results, while Table 1 summarizes the Jaccard similarity (JS) coefficient, Dice similarity (DS) coefficient, and CPU time (in seconds) of the main solver for each model. In this table, Image1 through Image6 correspond to the images shown in Fig. 9, listed from top to bottom, with the best performance highlighted in boldface. For two nonempty sets A and B, the JS and DS indices are defined as:

$$JS(A,B)=\frac{|A\cap B|}{|A\cup B|} \quad \text{and} \quad DS(A,B)=\frac{2|A\cap B|}{|A|+|B|}, \tag{5.1}$$

where $|S|$ denotes the cardinality of set S. Both coefficients range from 0 to 1, with higher values indicating greater similarity between sets A and B. In practice, we compute the JS and DS coefficients using the manual annotations as the ground truth, shown in Fig. 9(b), based on the corresponding more homogeneous images from Example 5.4, Fig. 8.

From the numerical results reported in Table 1, we observe that the proposed model (3.3) exhibits high performance and faster convergence compared to the other two selective segmentation models, SC and RCI. Notably, the SC and RCI models are primarily based on the Chan-Vese model [5], which assumes piecewise constant image intensity. This assumption may impact their segmentation accuracy for images with intensity inhomogeneity. In contrast, our model is derived from the LIC model [18], which is specifically designed to handle images with intensity inhomogeneity. On the other hand, the

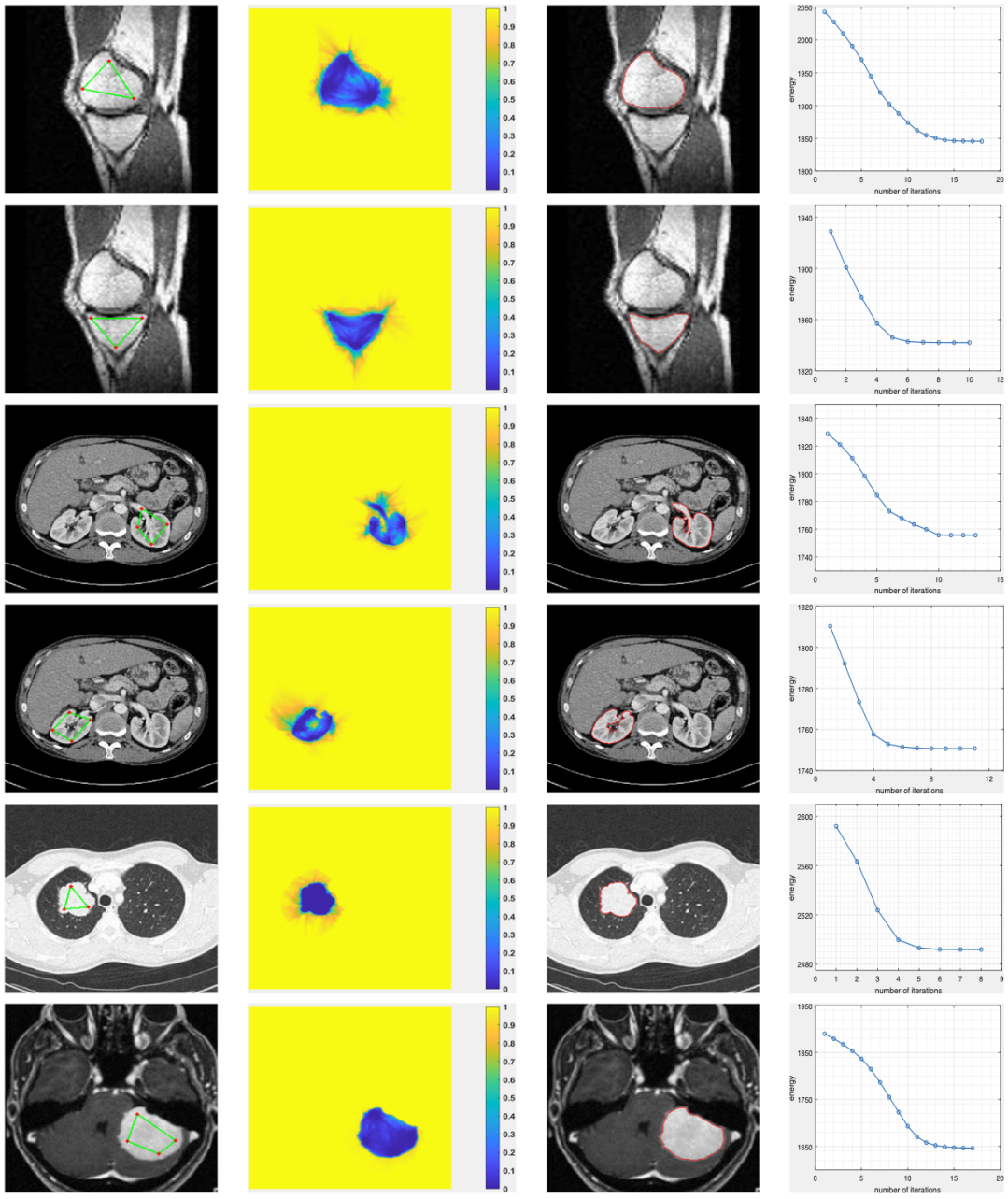

Figure 8: (Example 5.4) The selective segmentation results of the proposed method for six 256×256 medical images with slight intensity inhomogeneity: (a) source image f with marker points and initial characteristic function $\chi^{(0)}$; (b) TV distance function d; (c) segmentation results; (d) energy-decaying over ICT iterations.

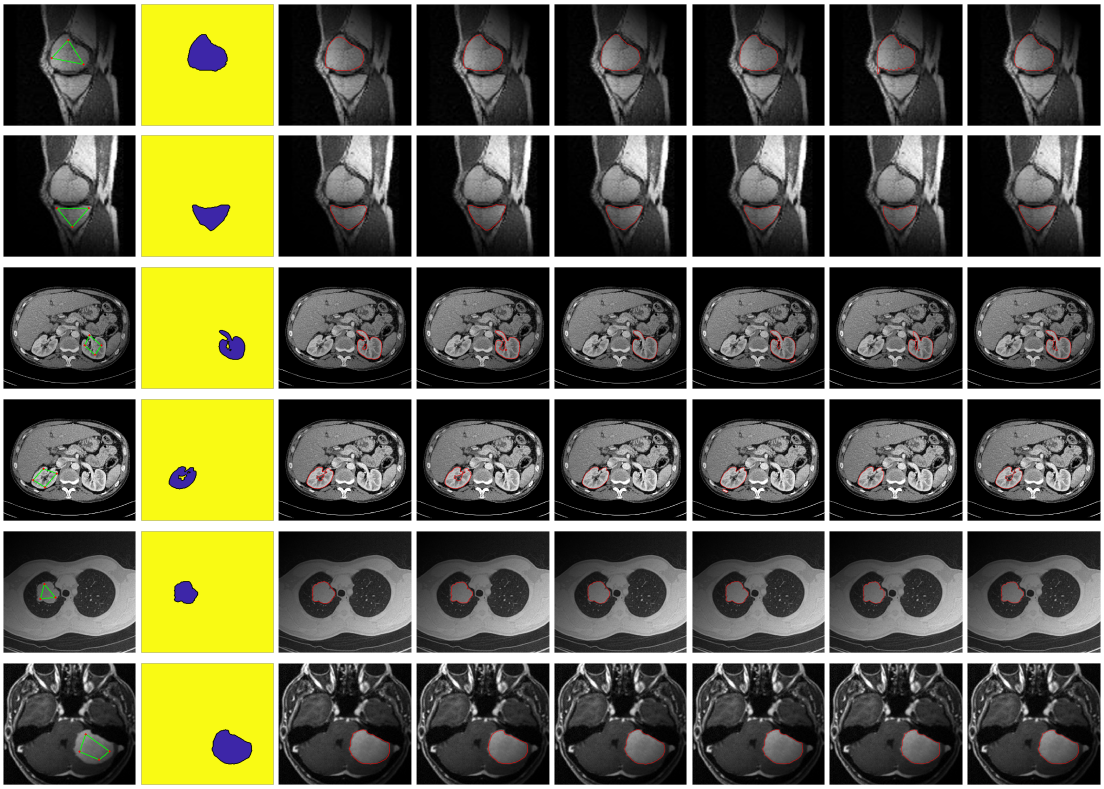

(a) $f(x)$ (b) GT (c) SC [36] (d) RCI [34] (e) PQMS [6] (f) LBF [19] (g) LSF [47] (h) Ours

Figure 9: (Example 5.5) The selective segmentation results of six 256×256 medical images with stronger intensity inhomogeneity: (a) source image f, where the marker points and initial characteristic function $\chi^{(0)}$ will be used in our model; (b) ground truth; (c) Spencer-Chen model [36]; (d) Roberts-Chen-Irion model [34]; (e) piecewise-quadratic Mumford-Shah model [6]; (f) local binary fitting energy model [19]; (g) local statistical fitting energy model [47]; (h) proposed model (3.3).

three global segmentation models–PQMS, LBF, and LSF–achieve reasonable segmentation results with fast convergence when implemented via the ICT method. However, due to their inherent global nature, they may fail to detect interior edges or over-segment non-target regions, even when the initial contour is placed sufficiently close to the target region. Despite this, we believe incorporating a similar area constraint term via the TV distance function can enhance these global segmentation models to achieve improved selective segmentation. Overall, as demonstrated in Fig. 9 and summarized in Table 1, the proposed approach proves to be well-suited for the selective segmentation of medical images affected by stronger intensity inhomogeneity.

Table 1: Comparisons of JS and DS coefficients and CPU time for different models in Example 5.5.

JS coefficient						
	SC [36]	RCI [34]	PQMS [6]	LBF [19]	LSF [47]	Ours
Image1	0.92	0.95	0.94	0.96	0.92	**0.98**
Image2	0.92	0.93	0.93	0.93	0.88	**0.94**
Image3	**0.92**	0.85	0.91	**0.92**	0.90	**0.92**
Image4	0.90	0.87	**0.91**	0.88	0.88	**0.91**
Image5	0.91	0.89	0.93	**0.97**	0.90	0.91
Image6	0.93	0.96	0.96	0.97	**0.98**	0.97
DS coefficient						
	SC [36]	RCI [34]	PQMS [6]	LBF [19]	LSF [47]	Ours
Image1	0.96	0.97	0.97	0.98	0.96	**0.99**
Image2	0.96	**0.97**	0.96	0.96	0.94	**0.97**
Image3	**0.96**	0.92	**0.96**	**0.96**	0.95	**0.96**
Image4	**0.95**	0.93	**0.95**	0.93	0.94	**0.95**
Image5	0.95	0.94	0.96	**0.98**	0.95	0.95
Image6	0.97	0.98	0.98	0.98	**0.99**	0.98
CPU time in seconds						
	SC [36]	RCI [34]	PQMS [6]	LBF [19]	LSF [47]	Ours
Image1	63.60	37.84	1.32	2.21	2.44	**1.00**
Image2	82.35	12.80	0.45	**0.17**	1.20	0.66
Image3	78.39	15.41	1.39	**0.56**	3.04	1.03
Image4	70.32	17.66	0.43	**0.19**	0.51	0.47
Image5	93.73	7.01	**0.31**	1.60	0.89	0.33
Image6	86.21	12.31	**0.64**	1.03	1.96	0.86

6 Summary and conclusions

In this paper, we proposed an enhanced local intensity clustering energy functional that incorporates a TV distance function to improve the selective segmentation of medical images, especially those with intensity inhomogeneity. The TV distance, derived from the SSR output, serves as an area constraint to accurately locate target objects. By combining this with local intensity clustering fitting energy and contour length regularization, our resultant model achieves precise selective segmentation. Instead of solving the Euler-Lagrange equation or employing the level set method, we introduced an efficient ICT method to numerically implement the model. This method ensures energy decay at each iteration and facilitates faster convergence. Numerical experiments demonstrated the effectiveness and efficiency of the proposed selective image segmentation approach.

In conclusion, this TV distance-enhanced fitting energy approach can be integrated with other region-based models, such as the Chan-Vese model [5] for intensity homogeneous images, as well as the local binary fitting energy model [19], the local statistical fitting energy model [47], and the piecewise-polynomial Mumford-Shah model [6] for intensity inhomogeneous images. Furthermore, recent advancements in deep unrolling techniques and variational loss functions [7,10,28] have enabled learning-based methods guided by variational models to develop more sophisticated structures, offer improved interpretability, reduce the need for extensive training data, and enhance performance. Thus, integrating our variational selective model with learning-based approaches to further strengthen segmentation performance is a promising direction for future research.

Acknowledgments

The authors thank the anonymous referees for their valuable comments and suggestions, which improved the quality of the paper. This work was partially funded by the National Science and Technology Council, Taiwan, under grants NSTC 112-2115-M-005-006-MY2 (P.-W. Hsieh) and NSTC 112-2811-M-008-043 (C.-L. Tseng), and by the Ministry of Science and Technology, Taiwan, under grant MOST 111-2115-M-008-006-MY3 (S.-Y. Yang).

References

[1] G. Aubert and P. Kornprobst, *Mathematical Problems in Image Processing: Partial Differential Equations and the Calculus of Variations, Second Edition,* Springer-Verlag, New York, 2006.
[2] N. Badshah and K. Chen, Image selective segmentation under geometrical constraints using an active contour approach, *Communications in Computational Physics,* 7 (2010), pp. 759-778.
[3] D. Batra, A. Kowdle, D. Parikh, J. Luo, and T. Chen, *Interactive Co-segmentation of Objects in Image Collections,* Springer, New York, 2011.
[4] V. Caselles, R. Kimmel, and G. Sapiro, Geodesic active contours, *International Journal of Computer Vision,* 22 (1997), pp. 61-79.
[5] T. F. Chan and L. A. Vese, Active contours without edges, *IEEE Transactions on Image Processing,* 10 (2001), pp. 266-277.
[6] C. Chen, J. Leng, and G. Xu, A general framework of piecewise-polynomial Mumford-Shah model for image segmentation, *International Journal of Computer Mathematics,* 94 (2017), pp. 1981-1997.
[7] K. Chen, C.-B. Schönlieb, X.-C. Tai, and L. Younes, *Handbook of Mathematical Models and Algorithms in Computer Vision and Imaging,* Springer Nature Switzerland AG, 2023.
[8] S. Esedoğlu and F. Otto, Threshold dynamics for networks with arbitrary surface tensions, *Communications on Pure and Applied Mathematics,* 68 (2015), pp. 808-864.
[9] C. Gout, C. Le Guyader, and L. Vese, Segmentation under geometrical conditions using geodesic active contours and interpolation using level set methods, *Numerical Algorithms,* 39 (2005), pp. 155-173.
[10] L. Gui, J. Ma, and X. Yang, Variational models and their combinations with deep learning in medical image segmentation: A survey, *Handbook of Mathematical Models and Algorithms in*

Computer Vision and Imaging, K. Chen et al. (Ed.), Springer Nature Switzerland AG, 2023, pp. 1001-1022.

[11] J. He, C.-S. Kim, and C.-C. J. Kuo, *Interactive Segmentation Techniques: Algorithms and Performance Evaluation,* Springer, New York, 2014.

[12] Z. Hou, A review on MR image intensity inhomogeneity correction, *International Journal of Biomedical Imaging,* 2006 (2006), pp. 1-11.

[13] P.-W. Hsieh, C.-L. Tseng, and S.-Y. Yang, Efficient variational segmentation with local intensity fitting for noisy and inhomogeneous images, *Multimedia Systems,* 30 (2024), Article 277.

[14] A. K. Jumaat and K. Chen, A reformulated convex and selective variational image segmentation model and its fast multilevel algorithm, *Numerical Mathematics: Theory, Methods and Applications,* 12 (2019), pp. 403-437.

[15] M. Jung, Piecewise-smooth image segmentation models with L^1 data-fidelity terms, *Journal of Scientific Computing,* 70 (2017), pp. 1229-1261.

[16] M. Kass, A. Witkin, and D. Terzopoulos, Snakes: active contour models, *International Journal of Computer Vision,* 1 (1998), pp. 321-331.

[17] E. H. Land, Recent advances in retinex theory, *Vision Research,* 26 (1986), pp. 7-21.

[18] C. Li, R. Huang, Z. Ding, J. C. Gatenby, D. N. Metaxas, and J. C. Gore, A level set method for image segmentation in the presence of intensity inhomogeneities with application to MRI, *IEEE Transactions on Image Processing,* 20 (2011), pp. 2007-2016.

[19] C. Li, C.-Y. Kao, J. C. Gore, and Z. Ding, Minimization of region-scalable fitting energy for image segmentation, *IEEE Transactions on Image Processing,* 17 (2008), pp. 1940-1949.

[20] X. Li, X. Yang, and T. Zeng, A three-stage variational image segmentation framework incorporating intensity inhomogeneity information, *SIAM Journal on Imaging Sciences,* 13 (2020), pp. 1692-1715.

[21] W.-T. Liao, S.-Y. Yang, and C.-S. You, An entropy-weighted local intensity clustering-based model for segmenting intensity inhomogeneous images, *Multimedia Systems,* 30 (2024), Article 49.

[22] C. Liu, Z. Qiao, and Q. Zhang, An active contour model with local variance force term and its efficient minimization solver for multiphase image segmentation, *SIAM Journal on Imaging Sciences,* 16 (2023), pp. 144-168.

[23] C. Liu, M. K.-P. Ng, and T. Zeng, Weighted variational model for selective image segmentation with application to medical images, *Pattern Recognition,* 76 (2018), pp. 367-379.

[24] J. Ma, D. Wang, X.-P. Wang, and X. Yang, A characteristic function-based algorithm for geodesic active contours, *SIAM Journal on Imaging Sciences,* 14 (2021), pp. 1184-1205.

[25] L. Min, X. Lian, Z. Jin, and M. Zheng, A Retinex-based selective segmentation model for inhomogeneous images, *Journal of Mathematical Imaging and Vision,* 65 (2023), pp. 437-452.

[26] M. Miranda, D. Pallara, F. Paronetto, and M. Preunkert, Short-time heat flow and functions of bounded variation in $\boldsymbol{R}^N$, *Annales de la Faculté des Sciences de Toulouse,* 16 (2007), pp. 125-145.

[27] A. Mitiche and I. B. Ayed, *Variational and Level Set Methods in Image Segmentation, Vol. 5,* Springer-Verlag, Berlin & Heidelberg, 2010.

[28] V. Monga, Y. Li, and Y. C. Eldar, Algorithm unrolling: interpretable, efficient deep learning for signal and image processing, *IEEE Signal Processing Magazine,* 38 (2021), pp. 18-44.

[29] D. Mumford and J. Shah, Optimal approximations by piecewise smooth functions and associated variational problems, *Communications on Pure and Applied Mathematics,* 42 (1989), pp. 577-685.

[30] A. B. Petro, C. Sbert, and J.-M. Morel, Multiscale Retinex, *Image Processing On Line,* 4 (2014), pp. 71-88.
[31] L. Rada and K. Chen, A new variational model with dual level set functions for selective segmentation, *Communications in Computational Physics,* 12 (2012), pp. 261-283.
[32] L. Rada and K. Chen, Improved selective segmentation model using one level-set, *Journal of Algorithms & Computational Technology,* 7 (2013), pp. 509-540.
[33] Y. Ren, D. Li, and L. Tang, A variational level set model based on additive decomposition for segmenting noisy images with intensity inhomogeneity, *Signal Processing,* 212 (2023), Article 109169.
[34] M. Roberts, K. Chen, and K. L. Irion, A convex geodesic selective model for image segmentation, *Journal of Mathematical Imaging and Vision,* 61 (2019), pp. 482-503.
[35] L. I. Rudin, S. Osher, and E. Fatemi, Nonlinear total variation based noise removal algorithms, *Physica D,* 60 (1992), pp. 259-268.
[36] J. Spencer and K. Chen, A convex and selective variational model for image segmentation, *Communications in Mathematical Sciences,* 13 (2015), pp. 1453-1472.
[37] L. Vese and T. Chan, A multiphase level set framework for image segmentation using the Mumford and Shah model, *International Journal of Computer Vision,* 50 (2002), pp. 271-293.
[38] U. Vovk, F. Pernuš, and B. Likar, A review of methods for correction of intensity inhomogeneity in MRI, *IEEE Transactions on Medical Imaging,* 26 (2007), pp. 405-421.
[39] L. Wang, L. He, A. Mishra, and C. Li, Active contours driven by local Gaussian distribution fitting energy, *Signal Processing,* 89 (2009), pp. 2435-2447.
[40] D. Wang and X.-P. Wang, The iterative convolution-thresholding method (ICTM) for image segmentation, *Pattern Recognition,* 130 (2022), Article 108794.
[41] D. Wang, H. Li, X. Wei, and X.-P. Wang, An efficient iterative thresholding method for image segmentation, *Journal of Computational Physics,* 350 (2017), pp. 657-667.
[42] L. Wang, C. Li, Q. Sun, D. Xia, and C.-Y. Kao, Active contours driven by local and global intensity fitting energy with application to brain MR image segmentation, *Computerized Medical Imaging and Graphics,* 33 (2009), pp. 520-531.
[43] X.-F. Wang, D.-S. Huang, and H. Xu, An efficient local Chan-Vese model for image segmentation, *Pattern Recognition,* 43 (2010), pp. 603-618.
[44] Y. Wu, M. Li, Q. Zhang, and Y. Liu, A Retinex modulated piecewise constant variational model for image segmentation and bias correction, *Applied Mathematical Modelling,* 54 (2018), pp. 697-709.
[45] H. Yu, F. He, and Y. Pan, A novel region-based active contour model via local patch similarity measure for image segmentation, *Multimedia Tools and Applications,* 77 (2018), pp. 24097-24119.
[46] K. Zhang, H. Song, and L. Zhang, Active contours driven by local image fitting energy, *Pattern Recognition,* 43 (2010), pp. 1199-1206.
[47] K. Zhang, L. Zhang, K.-M. Lam, and D. Zhang, A level set approach to image segmentation with intensity inhomogeneity, *IEEE Transactions on Cybernetics,* 46 (2016), pp. 546-557.